Facile One-Step Hydrothermal Fabrication of $(Sr_{0.6}Bi_{0.305})_2Bi_2O_7$/SnO$_2$ Heterojunction with Excellent Photocatalytic Activity

Di Zhu [1], **Xinling Wang** [1] , **Huiting An** [1], **Yan Zhong** [1,2], **Dianhui Wang** [1,2] , **Chengying Tang** [1,2] **and Chaohao Hu** [1,2,*]

[1]   School of Materials Science and Engineering, Guilin University of Electronic Technology, Guilin 541004, China; heyjude456@163.com (D.Z.); xlwang04@163.com (X.W.); ahq1399615134@163.com (H.A.); zyguet@163.com (Y.Z.); dhwang@guet.edu.cn (D.W.); ctang@guet.edu.cn (C.T.)

[2]   Guangxi Key Laboratory of Information Materials, Guilin University of Electronic Technology, Guilin 541004, China

*   Correspondence: chaohao.hu@guet.edu.cn

check for updates

Abstract: The pyrochlore-type $(Sr_{0.6}Bi_{0.305})_2Bi_2O_7$ (SBO), containing Bi^{3+} and Bi^{5+} mixed valent states, was recently found to be used as a new visible light responsive photocatalyst. Novel SBO/SnO$_2$ heterostructured composites were synthesized through a facile one-step hydrothermal method. The phase structure, morphology, chemical composition, and optical properties of the obtained samples were characterized by XRD, SEM, TEM, XPS, and UV-vis DRS. Compared to pure SBO and SnO$_2$, the synthesized SBO/SnO$_2$ composites exhibited significantly enhanced photocatalytic efficiency. The results indicated that the photoinduced holes and superoxide radicals play a dominant role and are the main reactive species during the degradation of Methylene Blue (MB) solution under visible light irradiation. Heterojunctions, formed in samples, directly contribute to the improvement of photocatalytic efficiency of SBO/SnO$_2$ composites, since it not only broadens the light response range, but also accelerates the separation of photogenerated carriers.

Keywords: $(Sr_{0.6}Bi_{0.305})_2Bi_2O_7$; $(Sr_{0.6}Bi_{0.305})_2Bi_2O_7$/SnO$_2$; hydrothermal method; heterojunction; photocatalytic activity

1. Introduction

Semiconductor-based photocatalysis has been considered one effective strategy to deal with global environmental pollution and the energy crisis [1–4]. TiO$_2$ has been extensively studied as a popular photocatalyst since the photocatalytic splitting of water on TiO$_2$ photochemical electrodes was first reported in 1972 [5]. However, the relatively large band gap of about 3.2 eV for the anatase TiO$_2$ and low quantum efficiency directly limit its wider practical applications [6]. In recent years, many researchers have devoted a lot of effort to developing new visible light responsive photocatalysts [7–11].

Recently, a series of bismuth-based semiconductor photocatalysts have drawn much attention, owing to their special crystal structure and electronic structure. Many Bi^{3+}-containing semiconductor compounds like Bi$_2$O$_3$ [12], Bi$_2$WO$_6$ [13], BiVO$_4$ [14], BiOX (X = Cl, Br, I) [15,16], Bi$_2$SnO$_7$ [17], and Bi$_2$O$_2$CO$_3$ [18] have been found to exhibit high photocatalytic activity, driven by visible light, owing to the hybridization of O-2p and filled Bi-6s orbitals. Some Bi^{5+}-containing compounds such as NaBiO$_3$ [19], KBiO$_3$ and MgBi$_2$O$_6$ [20] also possess excellent photocatalytic performance due to the contribution from the Bi-5d and O-2p orbitals. In addition, recent studies [21,22] have indicated that Bi$_2$O$_4$ containing the mixed valent states of Bi (Bi^{3+} and Bi^{5+}) can serve as an important visible light

responsive photocatalyst with much higher photocatalytic degradation activity in comparison to some well-investigated, highly efficient photocatalysts.

In fact, $(Sr_{0.6}Bi_{0.305})_2Bi_2O_7$ (SBO) can also be considered one kind of special Bi-based oxides with Bi^{3+} and Bi^{5+} mixed valent states. Moreover, it possesses the cubic pyrochlore-type structure similar to that of $Bi_2Sn_2O_7$. In SBO, some Bi^{3+} and Bi^{5+} ions locate at the 16*c* sites (Wyckoff representation), Sr^{2+} and another part of Bi^{3+} ions, as well as a small amount of vacancies that occupy the 16d sites. While the synthesis and structural characterization of SBO have been previously reported [23], its chemical catalytic property has not attracted enough attention to date. Very recently, we have successfully fabricated the SBO compound via the hydrothermal method and found that SBO can photodegrade various organic dyes and possesses visible light photocatalytic activity [24]. However, the band gap of SBO is relatively small at about 1.25 eV, and quick recombination of photoinduced electrons and holes readily occur, undoubtedly affecting its photocatalytic efficiency [25,26].

Currently, the construction of heterojunctions with multiple functional components has been considered to be an extremely effective pathway to improve the photocatalytic activity of semiconductor photocatalysts, since not only the light absorption in the heterostructured composites is significantly enhanced, but the separation and transportation of photogenerated charge carriers are also effectively promoted [27–29]. Tin dioxide (SnO_2) has a relatively large band gap of about 3.8 eV and fails to absorb light with wavelengths over 330 nm [29]. However, a great amount of research on SnO_2-related heterojunctions, via coupling with other semiconductors like TiO_2 [30], ZnO [31], BiOI [32], and NiO [33], has verified the significantly enhanced photocatalytic activity of composites.

In this work, we devoted a lot of effort to synthesizing the SBO/SnO_2 heterostructured composites through a facile one-step hydrothermal method. The phase structure, morphology, microstructure, and optical property of the as-prepared composites were characterized by various experimental techniques. The photocatalytic activity of SBO/SnO_2 heterojunctions driven by visible light was estimated by the photochemical degradation of MB dye. Moreover, the mechanism for the enhancement of photocatalytic efficiency for the composite catalysts was proposed by trapping the free radicals' experiments and relative photoelectrochemical measurements.

2. Materials and Methods

2.1. Materials

The chemicals for synthesis were used in this paper with an analytical purity, and were purchased from Beijing Chemical Reagents Industrial Company of China. All the solutions were prepared with deionized water.

2.2. Preparation of Photocatalysts

In this paper, a facile one-step hydrothermal method for the synthesis of the SBO/SnO_2 composite samples was used. 0.5 mmol of $NaBiO_3 \cdot 2H_2O$ and 1 mmol of $Sr(NO_3)_2$ were, respectively, dissolved in 30 mL of deionized water under vigorous stirring for 10 min at room temperature to prepare solution A and B, respectively. Brown-yellow solution C was further obtained by mixing solution A and B, and by being stirred for about 30 min at room temperature. Subsequently, different contents (1.46 g, 1.21 g, 1.04 g, 0.81 g and 0.728 g) of SnO_2 were, respectively, added in the five identical portions of solution C, and the pH value was adjusted to 12 by adding 4 M NaOH. The mixture solution was then transferred to a 100 mL of a Teflon-lined stainless autoclave and heated at 140 °C for 6 h in a drying oven. After the hydrothermal reaction, the as-obtained sample was filtered, washed several times with deionized water and absolute ethanol, and finally dried at 60 °C for 12 h. The resultant composites were denoted as 10 wt% SBO/SnO_2, 12 wt% SBO/SnO_2, 14 wt% SBO/SnO_2, 18 wt% SBO/SnO_2 and 20 wt% SBO/SnO_2 with the color change from light gray to dark gray, respectively. Pure SBO was also prepared by the same process as the preparation of the samples without SnO_2.

2.3. Characterization

A powder X-ray diffractometer (XRD, Bruker D8-Advance, Germany) was used to characterize the crystal structure of as-synthesized samples. A field-emission scanning electron microscope (FE-SEM, Hitachi, Tokyo, Japan) with an energy dispersive X-ray spectroscopy (EDS) was used to characterize the morphologies and elemental analyses of samples. The microstructures of the samples were further measured on the transmission electron microscopy (TEM, FEI Tecnai G20, Hillsboro, OR, USA), operating at 200 kV. The X-ray photoelectron spectroscopy (XPS) measurement was carried out by using an Escalab 250Xi system with a Al Kα radiation source (1486.6 eV). Fourier transform infrared (FT-IR) spectra were recorded on a FTIR spectrometer (Thermo Fisher Nicolet 6700, Waltham, MA, USA) using the standard KBr disk method. The UV-Vis diffuse reflectance spectra (UV-Vis DRS, Puxi TU-1901, Beijing, China) of the as-prepared photocatalysts were measured with a UV-Vis spectrometer (Puxi TU-1901, Beijing, China), in the range of 230–750 nm, using $BaSO_4$ as a reference.

2.4. Determination of Photocatalytic Activity

The photocatalytic performance of the obtained samples was evaluated by degrading the MB solution under visible light irradiation. A 300 W xenon lamp was used as the light source, and a UV-cut filter was used to remove the wavelength of light below 400 nm. In detail, 0.2 g of the powdered catalyst was dispersed into 100 mL of MB aqueous solution (10 mg/L) in a quartz beaker. Before irradiation, the resultant mixture was stirred in the dark for 30 min in order to achieve an adsorption–desorption equilibrium between the MB dye and photocatalysts. 3 mL of the mixture was collected at regular intervals and was immediately filtered to remove the catalysts. Subsequently, the remnant concentration of MB at different intervals was determined by measuring the photocatalytic degradation ratio using a Puxi TU-1901 UV-Vis spectrophotometer.

2.5. Photoelectrochemical Measurement

The measurement of electrochemical impedance spectra (EIS) for the as-prepared photocatalysts was performed on an electrochemical workstation (Parstat MC, Princeton Applied Research, Delaware, DE, USA) in a conventional three-electrode cell, with an Ag/AgCl electrode, the prepared samples, and a Pt plate as the reference electrode, the working electrode, and the counter electrode, respectively. An aqueous solution containing 0.5 M KOH was chosen as the electrolyte. A 300 W xenon lamp (CEL-HXF300, Aulight, Beijing, China), equipped with an AM 1.5G filter, was used as the visible light source. Nyquist plots were measured in the frequency range from 0.1 Hz to 100 kHz with a voltage amplitude of 10 mV. The transient photocurrent response of samples was measured on a Keysight B1500A semiconductor device analyzer and an Advanced PW-600 probe station. The waveform generator was used to monitor the pulse frequency and optical power determined by an Ophir Nova II handheld laser power/energy meter.

3. Results and Discussion

3.1. Phase Structure and Chemical Compositions

Figure 1 presents the XRD patterns of as-synthesized SBO, SnO_2, and SBO/SnO_2 nanocomposites with different mass ratios. The typical diffraction peaks at 2θ = 26.5°, 33.8°, 37.9°, 51.7°, 54.7°, 57.8°, 61.9°, 64.7°, 65.9° and 78.6° can be readily assigned to the standard card of tetragonal SnO_2 (JCPDS no. 99-0024). The characteristic diffraction peaks at 2θ = 28.1°, 32.5°, 46.6°, 55.3°, 58.0°, and 75.2° are well indexed to the (222), (400), (440), (622), (444), and (662) lattice planes of the pyrochlore-type SBO (JCPDS card no. 81-2460). The diffraction peaks of SBO and SnO_2 can be observed in the XRD patterns of SBO/SnO_2 composites. The sharp and narrow peaks indicate that the obtained SBO/SnO_2 composites have high crystallinity. Moreover, no other peaks from possible impurities are detected in these patterns. It can also be found that, when the content of SBO is about 10 wt%, the diffraction peaks of SBO are not obvious in the 10 wt% SBO/SnO_2 composite, except the peak corresponding to

the (400) lattice plane, which can be observed. As the concentration of SBO further increases in the composites, the characteristic diffraction peaks of SBO become stronger. However, the measured XRD patterns show that the intensity of all the peaks of SnO_2 in the composites is decreased gradually by further increasing the content of SBO to higher than 14 wt%.
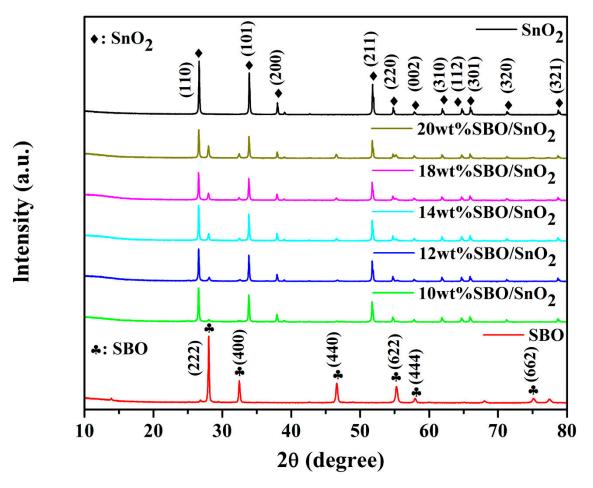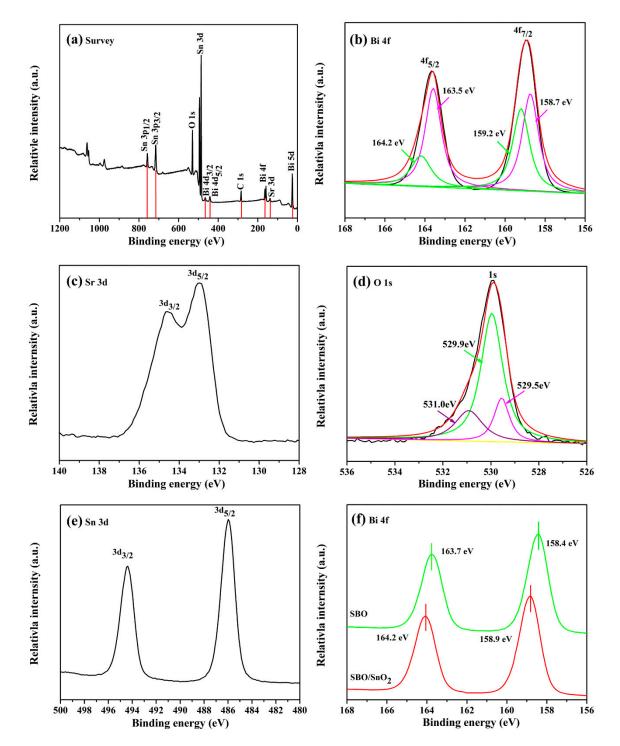

Figure 1. XRD patterns of SnO_2, SBO, and SBO/SnO_2 composites containing 5 wt%, 10 wt%, 14 wt%, 18 wt%, and 20 wt% of SBO, respectively.

The measured XPS shown in Figure 2 is used to further investigate the oxidation state and surface chemical compositions of as-prepared composites. The full scan spectrum presented in Figure 2a reveals the presence of Bi, O, Sr, and Sn elements in the as-prepared samples. The peak of C1s at 284.6 eV in the spectrum was assigned to the adhesive hydrocarbons from the XPS instrument itself. The Bi 4f spectra of 14 wt% SBO/SnO_2 shown in Figure 2b indicate that the peak of Bi $4f_{7/2}$ (or Bi $4f_{5/2}$) can be well deconvoluted into two peaks at binding energy of 158.7 and 159.2 eV [34] (or at 163.5 and 164.2 eV), which is attributed to Bi^{3+} and Bi^{5+} [35] and accords well with the previous results on the Bi_2O_4-based systems [36,37]. The peaks at binding energy of 132.9 and 134.7 eV shown in Figure 2c are, respectively, assigned to Sr $3d_{5/2}$ and Sr $3d_{3/2}$ of Sr^{2+} [38]. For the spectrum of O 1s presented in Figure 2d, the binding energy around 529.5 eV corresponds to the lattice oxygen of Sr-O or Bi-O bonds, which is comparable to our previous measurements on $Bi_2Sn_2O_7$ and $MgBi_2O_6$ [39]. The peaks at 531.0 and 529.9 eV are ascribed to the physically adsorbed oxygen and chemisorbed oxygen, respectively [40]. The characteristic XPS peaks of Sn 3d presented in Figure 2e are located at 494.4 and 486.0 eV and correspond to Sn $3d_{3/2}$ and Sn $3d_{5/2}$ of Sn^{4+}. In addition, it can be found from Figure 2f that an apparent drift of binding energy exists in 14 wt% SBO/SnO_2, in comparison to pure SBO. This may be attributed to the change in internal electron density caused by the formation of the

SBO/SnO_2 heterojunction. Similar phenomena have been previously reported in the $Bi_2O_2CO_3/g$-C_3N_4 heterostructured composite [18].

Figure 2. XPS spectra of 14 wt% SBO/SnO_2 composite: (**a**) full scan survey of all elements and high-revolution spectra of (**b**) Bi 4f, (**c**) Sr 3d, (**d**) O 1s, (**e**) Sn 3d, and (**f**) Bi 4f of pure SBO for comparison.

3.2. Morphology Analysis

The typical FE-SEM images of pure SBO, SnO_2, and 14 wt% SBO/SnO_2 composite, together with the EDS elemental mapping, are shown in Figure 3. As presented in Figure 3a, the pure SBO sample consists of large numbers of irregular blocks with sizes from about 0.1 to 0.4 μm. Figure 3b shows that

the size distribution of SnO_2 particles is wider and in the range of 0.04–0.6 μm, although the pure SnO_2 sample has a similar morphology to SBO. It can be seen from Figure 3c,d that the size distribution of as-prepared SBO/SnO_2 composite particles is also non-uniform. However, the sizes of SBO and SnO_2 particles in SBO/SnO_2 are markedly reduced after one-step hydrothermal synthesis and SnO_2 particles with smaller size are strongly anchored on the surface of the SBO particles. The EDS elemental mapping of the 14 wt% SBO/SnO_2 composite presented in Figure 3e further shows the distribution of SnO_2 particles on the relatively larger SBO particles. The EDS spectrum of 14 wt% SBO/SnO_2, shown in Figure 3f, confirms the peaks of Bi, Sr, O and Sn elements, indicating the existence of SBO and SnO_2 components in the as-prepared composite.
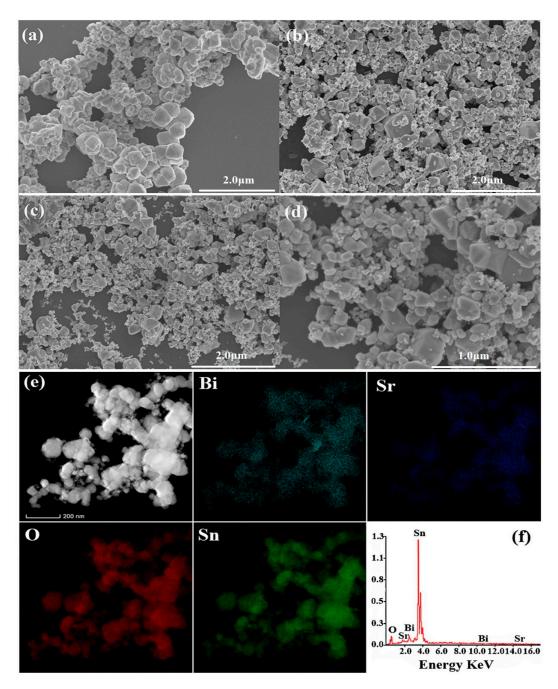

Figure 3. FESEM images of (**a**) SBO, (**b**) SnO_2, (**c**) and (**d**) 14 wt% SBO/SnO_2 composite, (**e**) Energy Dispersive Spectrometer (EDS) elemental mapping and (**f**) EDS spectrum of 14 wt% SBO/SnO_2 composite.

TEM and high-resolution TEM (HRTEM) images were employed to further investigate the morphological structure of the 14 wt% SBO/SnO$_2$ composite. As shown in Figure 4a,b, SnO$_2$ particles are deposited randomly on the surface of SBO particles with an obviously larger size. HRTEM images presented in Figure 4c,d show that the clear lattice fringes with the interplanar distance of 0.3178 and 0.2644 nm corresponding to the (222) lattice plane of SBO and the (101) lattice plane of SnO$_2$, respectively. Moreover, the distinguished interfaces between SBO and SnO$_2$ are well built and contact tightly with each other, which strongly indicates the formation of the heterojunction between SBO and SnO$_2$.
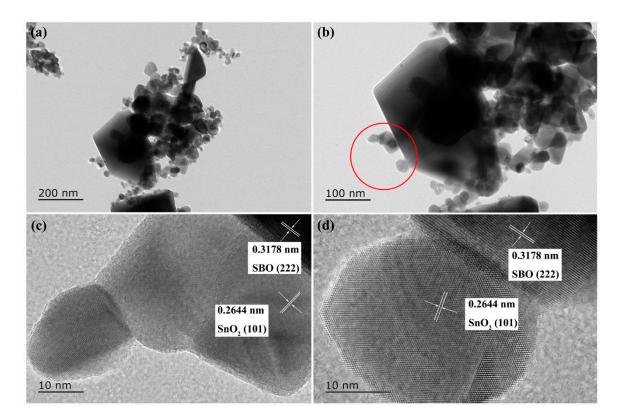

Figure 4. Transmission Electron Microscope (**a,b**) and High Resolution Transmission Electron Microscope (**c,d**) images of 14 wt% SBO/SnO$_2$ composite.

3.3. Optical Absorption Properties of SBO/SnO$_2$ Catalysts

Figure 5 exhibits the typical UV-vis diffuse reflectance spectra (DRS) of pure SBO, SnO$_2$ and 14 wt% SBO/SnO$_2$ composites. The absorption edge of SnO$_2$ is at about 356 nm and can only absorb the UV light, while the UV-vis DRS of pure SBO shows a long absorption tail in the range of 400–800 nm due to a darker hue. Compared to pure SnO$_2$, the UV-vis DRS of 14 wt% SBO/SnO$_2$ has a redshift, and the corresponding absorption edge is about 367 nm. The band gap of as-prepared photocatalysts can be estimated by the formula, $(\alpha h v)^n = A(h v - E_g)$, where h, α, E_g, v, and A are the Plank constant, absorption coefficient, band gap, light frequency, and a constant, and the value of n depends on the type of optical transition in semiconductor. $n = 2$ is for direct transition and $n = 1/2$ is for indirect transition. The values of n for SBO and SnO$_2$ are equal to 2, since they are direct semiconductors. The E_g of SBO and SnO$_2$ estimated from the plot of $(\alpha h v)^2$, as a function of photon energy, are 1.25 and 3.60 eV, which are consistent with the previously reported values [24,30,34]. Considering the color of the prepared 14 wt% SBO/SnO$_2$ composite, here we assume that it is an indirect semiconductor. The estimated E_g of 14 wt% SBO/SnO$_2$ from the plot of $(\alpha h v)^{1/2}$ as a function of photon energy is about 2.96 eV, which indicates that, in the visible light region, the 14 wt% SBO/SnO$_2$ composite has a stronger absorption ability than SnO$_2$ and is favorable for photocatalytic reactions.
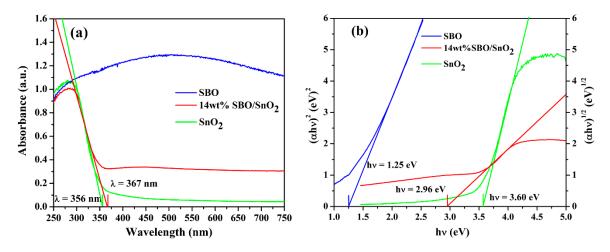
Figure 5. (**a**) UV-vis diffuse reflectance spectra and (**b**) the band gap energy of SBO, SnO_2, and 14 wt% SBO/SnO_2 composite.

3.4. Photocatalytic Activity and Stability

The photocatalytic activities of SBO, SnO_2 and SBO/SnO_2 composites with different concentrations of SBO were investigated by the degradation of MB dye solution under the illumination of visible light ($\lambda > 420$ nm). As presented in Figure 6a, the blank test shows that, after 60 min reaction, no MB is removed without catalysts, indicating that the degradation of MB is driven by photocatalysis. Pure SBO and SnO_2 show poor photocatalytic activity and can only degrade about 22.1% and 34.2% of MB after 60 min visible light irradiation, respectively. SBO/SnO_2 composite catalysts obviously exhibit the increased photocatalytic efficiency of MB in comparison to pure SBO and SnO_2. In particular, tge 14 wt% SBO/SnO_2 composite displays the highest removal efficiency of MB (93.2%). However, the removal efficiency of MB is gradually decreased with the concentration of SBO beyond 14 wt%, because the excessive black SBO can probably screen the active sites on the surface of catalysts. Therefore, it is important to control the content of SBO in the composites in order to significantly enhance the photocatalytic performance. In addition, we can find that the degradation efficiency of MB over the 14 wt% SBO/SnO_2 simple physical mixture is obviously slower than that of the composites. This strongly confirms the successful fabrication of SBO/SnO_2 heterostructured photocatalysts in our current work. A comparative experiment on the degradation of MB over 14 wt% SBO/SnO_2 under only the UV light illumination using a 300 W xenon lamp with the UVREF filter ($\lambda < 400$ nm) is also carried out. The measured results indicate that, under visible light illumination, the composite catalyst has only a slightly lower degradation efficiency than the same catalyst under UV light illumination. This clearly shows that the decomposition of MB, resulting from the visible light excitation, can be ignored. In addition, the degradation efficiency of MB over the 14 wt% SBO/SnO_2 is comparable with other bismuth compounds or SnO_2 based composites. For example, Yin et al. found that $SnO_2/BiVO_4$ composite catalysts showed remarkably improved visible-induced photocatalytic activity and the MB solution can be completely degraded under 120 min visible light irradiation [41].

Figure 6b shows that the photodegradation of the MB solution over pure SBO, SnO_2, and SBO/SnO_2 composites is the first-order reaction and the kinetics can be expressed using the following formula, $-\ln(C/C_0) = kt$ (C_0 is the concentration of dye after building the adsorption-desorption equilibrium, C is the reaction concentration at any time, k is the pseudo-first-order rate constant for degradation of dye, and t is the illumination time). It can be found that the value of k for MB degradation over 14 wt% SBO/SnO_2 is about 0.0581 min^{-1} and is, respectively, 15.6 and 7.3 times higher than those of pure SBO and SnO_2. Therefore, the results clearly show the obviously enhanced photocatalytic performance of SBO/SnO_2 heterojunctions in comparison to pure SBO and SnO_2. Figure 6c shows the temporal change of the absorption spectra in the degradation of MB dye over 14 wt% SBO/SnO_2 within the time interval of 10 min under visible light irradiation. MB has a major absorption peak at around 664 nm. The peak

intensity of MB, at around 664 nm, decreases to zero after 60 min irradiation, indicating the complete degradation of MB solution.
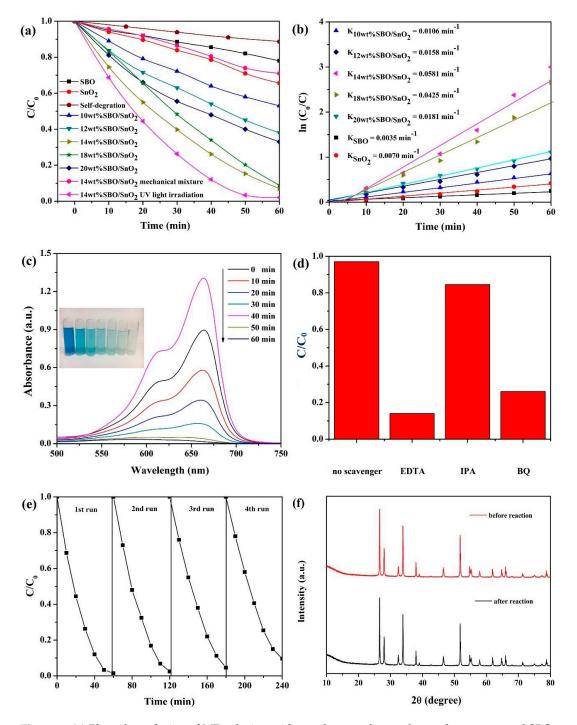

Figure 6. (**a**) Photodegradation of MB solution without photocatalyst and over the as-prepared SBO, SnO_2, and SBO/SnO_2 with different concentration of SBO; (**b**) kinetic plot of the photodegradation of MB solution versus irradiation time; (**c**) temporal absorption spectra of MB solution in the presence of 14 wt% SBO/SnO_2; (**d**) degradation of MB over 14 wt% SBO/SnO_2 in the presence of different scavengers; (**e**) cycling runs of 14 wt% SBO/SnO_2 for MB degradation; and (**f**) XRD patterns of 14 wt% SBO/SnO_2 before and after a four-cycle reaction.

The free radical trapping experiments are further carried out to investigate the main types of reactive species like superoxide radical ($\bullet O_2^-$), hydroxyl radical ($\bullet OH$), and hole (h^+) during the

photodegradation of MB dye over SBO/SnO$_2$ composites. In our work, the 5 mmol of benzoquinone (BQ), isopropanol (IPA), and ethylenediamine tetraacetic acid (EDTA) are used as the scavenger of •O$_2^-$, •OH, and h$^+$, respectively. It can be found from Figure 6d that the degradation efficiency of the MB solution is obviously decreased when EDTA and BQ scavengers are added. This strongly indicates that the photoinduced •O$_2^-$ and h$^+$ are the main reactive species in the photochemical reaction and play a crucial role for the degradation of MB. On the contrary, adding IPA almost does not suppress the degradation of MB solution, indicating that •OH is the secondary reactive species during the photochemical reaction.

The stability of photocatalysts is of great importance to their practical application. Figure 6e presents the cycling measurements, reflecting the long-term stability of 14 wt% SBO/SnO$_2$ composite. It can be found that 14 wt% SBO/SnO$_2$ does not show a distinct decrease in the photocatalytic activity after four cycles. As shown in Figure 6f, moreover, the crystal structure and phase composition of 14 wt% SBO/SnO$_2$ do not change after a four-cycle photocatalytic reaction. Thus, we can see that the as-prepared SBO/SnO$_2$ composites possess excellent structural stability under visible light illumination.

3.5. Possible Photocatalytic Mechanism

As clearly shown in Figure 6, the as-prepared SBO/SnO$_2$ heterostructured composites exhibit higher visible light photocatalytic performance than pure SBO and SnO$_2$. The EIS Nyquist plots and transient photocurrent responses of pure SBO, SnO$_2$, and 14 wt% SBO/SnO$_2$ composite are further measured to investigate the migration, transfer and recombination processes of photoinduced holes and electrons. It is a well-known fact that the Nyquist curve is a semicircle when the charge transfer is a decisive step. The relative size of the arc radius of Nyquist plots corresponds to the separation efficiency of light-excited carriers. Generally, the smaller the arc radius of the impedance spectrum is, the higher the separation efficiency of light-excited carriers is, and the faster the photocatalytic reaction is [42,43]. As presented in Figure 7a, the arc radius of EIS plot of 14 wt% SBO/SnO$_2$ is obviously smaller than those of pure SBO and SnO$_2$, which means that the as-synthesized SBO/SnO$_2$ possesses a faster charge transfer process at the interface and more effective separation efficiency of photoinduced carriers than pure SBO and SnO$_2$. The measured photocurrent responses of catalysts presented in Figure 7b further verify that SBO/SnO$_2$ heterostructured composites are more effective in separating the photogenerated carriers, in comparison to pure SBO and SnO$_2$, since the photocurrent density generated by SBO/SnO$_2$ is obviously larger than that generated by pure SBO and SnO$_2$.
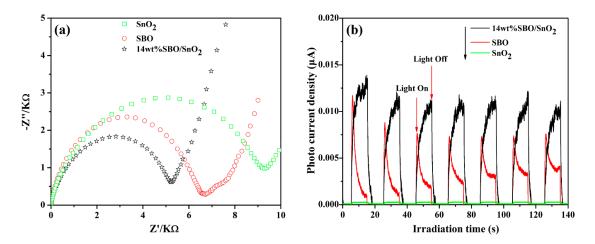

Figure 7. (**a**) Electrochemical impedance Spectroscopic plots and (**b**) transient photocurrent response of pure SnO$_2$, SBO, and 14 wt% SBO/SnO$_2$ heterojunction.

Figure 8 schematically illustrates the possible mechanism of the photocatalytic degradation of MB by SBO/SnO$_2$ composites. The enhanced photocatalytic activity of SBO/SnO$_2$ composites could

result from the charge transfer process between SBO and SnO_2. The band edge position is the key to determining the separation of photoinduced charge carriers in the heterostructured composite. The band edge positions of SBO and SnO_2 can be obtained from the following empirical formula [44]:

$$E_{VB} = 1/2E_g + X - E_e \tag{1}$$

$$E_{CB} = E_{VB} - E_g \tag{2}$$

where E_{VB} and E_{CB} are the valence and conduction band edge potentials, X and E_e represent the electronegativity of a semiconductor and the energy of free electrons (approximately 4.5 eV), respectively. The calculated values of X for SBO and SnO_2 are 5.80 and 6.25 eV, respectively. Then the estimated E_{CB} and E_{VB} of SBO are 0.68 and 1.93 eV, and $E_{CB} = -0.05$ eV and $E_{VB} = 3.55$ eV are for SnO_2. The CB of both SBO and SnO_2 are more positive than the standard $O_2/\bullet O_2^-$ redox potential (-0.33 eV vs. NHE) [45], which indicates that the electrons excited in the CB of SBO or SnO_2 cannot reduce O_2 molecules into the strong oxidizing $\bullet O_2^-$. The position of the Fermi level of n-type SBO is normally different from that of n-type SnO_2. As shown in Figure 8, after the charge equilibrium is built, the Fermi level of SBO move up heavily and that of SnO_2 move down slightly, and the n-n heterojunction is finally formed. Now the reduction of O_2 into $\bullet O_2^-$ becomes feasible, since the CB of SBO/SnO_2 heterostructured composite will become more negative. Furthermore, the h^+ photoinduced on the VB of SBO has strong oxidizing activity and can directly oxidize dye molecules. Considering the fact that the VB of SBO are more negative than the standard $\bullet OH/H_2O$ redox potential (1.99 eV vs. NHE) [46], we can infer that the h^+ on the VB of SBO cannot oxidize OH^- into $\bullet OH$. Additionally, SnO_2 cannot be excited to produce the holes and electrons under visible light illumination, owing to its relatively large E_g of about 3.60 eV. Based on the discussion above, we can ascribe the decoloration of the MB solution to the reaction with h^+ and $\bullet O_2^-$ during photocatalysis, which has been verified by the trapping experiments of the active species presented in Figure 6d. Therefore, the efficient photodegradation progress of MB over SBO/SnO_2 composites can be described as follows,

$$SBO + h\nu \text{ (visible)} \rightarrow SBO \text{ } (h^+@VB + e^-@CB) \tag{3}$$

$$SBO \text{ } (e^-@CB) \rightarrow SnO_2 \text{ } (e^-@CB) \tag{4}$$

$$SnO_2 \text{ } (e^-@CB) + O_2 \rightarrow \bullet O_2^- \tag{5}$$

$$h^+ + \bullet O_2^- + dye \rightarrow \text{Degraded products} \tag{6}$$

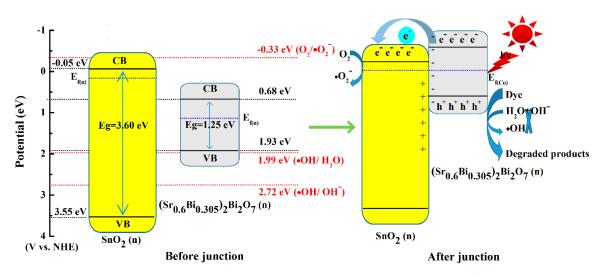**Figure 8.** Possible mechanism of photocatalytic activity of SBO/SnO_2 heterojunction for the degradation of MB under visible light irradiation.

4. Conclusions

$(Sr_{0.6}Bi_{0.305})_2Bi_2O_7$ (SBO) with the pyrochlore-type crystal structure belongs to one kind of special compound containing a small amount of vacancies and can be considered a potential semiconductor photocatalyst since it contains mixed valent states of Bi (Bi^{3+} and Bi^{5+}) such as Bi_2O_4 with high photocatalytic degradation efficiency. In this work, SBO/SnO_2 composites were first successfully synthesized via the facile one-step hydrothermal method. The characterizations of the phase structure, morphology, microstructure, and optical properties clearly showed the formation of heterojunction between SBO and SnO_2 in the as-prepared composites. The fabricated SBO/SnO_2 heterojunctions possessed the significantly enhanced photocatalytic performance towards MB degradation in comparison to pure SBO and SnO_2. The trapping experiments showed that the photogenerated $\bullet O_2^-$ and h^+ are the major reactive species and play a vital role during the photodegradation of MB solution. The measured EIS and transient photocurrent responses demonstrated that the significantly enhanced catalytic efficiency of SBO/SnO_2 nanocomposites is mainly attributed to the broad photoresponse range and efficient separation of photoinduced electron-hole pairs owing to the formation of heterojunction in the as-prepared composites.

Author Contributions: Conceptualization, C.H. and Y.Z.; methodology, Y.Z.; software, D.W.; validation, D.Z., H.A. and C.T.; formal analysis, D.Z.; investigation, D.Z. and X.W.; resources, C.H.; data curation, D.Z. and H.A.; writing—original draft preparation, D.Z. and X.W.; writing—review and editing, C.T., D.W. and C.H.; visualization, D.Z. and X.W.; supervision, C.H. and Y.Z.; project administration, C.H.; funding acquisition, C.H. All authors have read and agree to the published version of the manuscript.

Conflicts of Interest: The authors declare no conflict of interest.

References

1. Chen, C.; Ma, W.; Zhao, J. Semiconductor-mediated photodegradation of Pollutants under visible-light irradiation. *Chem. Soc. Rev.* **2010**, *39*, 4206–4219. [CrossRef]

2. Li, H.; Zhou, Y.; Tu, W.; Ye, J.; Zou, Z. State-of-the-art progress in diverse heterostructured photocatalysts toward promoting photocatalytic performance. *Adv. Funct. Mater.* **2015**, *25*, 998–1013. [CrossRef]

3. Kowalska, E.; Yoshiiri, K.; Wei, Z.S.; Zheng, S.Z.; Kastl, E.; Reita, H.; Ohtani, B. Hybrid photocatalysts composed of titania modified with plasmonic nanoparticles and ruthenium complexes for decomposition of organic compounds. *Appl. Catal. B Environ.* **2015**, *178*, 133–143. [CrossRef]

4. Huang, Y.; Fan, W.; Long, B.; Li, H.; Zhao, F.; Liu, Z.; Tong, Y.; Ji, H. Visible light $Bi_2S_3/Bi_2O_3/Bi_2O_2CO_3$ photocatalyst for effective degradation of organic pollutions. *Appl. Catal. B Environ.* **2016**, *186*, 68–76. [CrossRef]

5. Fujishima, A.; Honda, K. Electrochemical photolysis of water at a semiconductor electrode. *Nature* **1972**, *238*, 37–38. [CrossRef]

6. Zhang, X.; Wang, Y.; Liu, B.; Sang, Y.; Liu, H. Heterostructures construction on TiO_2 nanobelts: A powerful tool for building high-performance photocatalysts. *Appl. Catal. B Environ.* **2017**, *202*, 620–641. [CrossRef]

7. Yi, Z.G.; Ye, J.H.; Kikugawa, N.; Kako, T.; Ouyang, S.X.; Stuart-Williams, H.; Yang, H.; Cao, J.Y.; Luo, W.J.; Li, Z.S.; et al. An orthophosphate semiconductor with photooxidation properties under visible-light irradiation. *Nat. Mater.* **2010**, *9*, 559–564. [CrossRef] [PubMed]

8. Kumar, S.G.; Devi, L.G. Review on modified TiO_2 photocatalysis under Uv/visible light: Selected results and related mechanisms on interfacial charge carrier transfer dynamics. *J. Phys. Chem. A* **2011**, *115*, 13211–13241. [CrossRef] [PubMed]

9. Tian, J.; Zhao, Z.; Kumar, A.; Boughton, R.I.; Liu, H. Recent progress in design, synthesis, and applications of one-dimensional TiO_2 nanostructured surface heterostructures: A review. *Chem. Soc. Rev.* **2014**, *43*, 6920–6937. [CrossRef]

10. Cao, S.; Yu, J. g-C$_3$N$_4$-Based photocatalysts for hydrogen production. *J. Phys. Chem. Lett.* **2014**, *5*, 2101–2107. [CrossRef]

11. Zhang, L.; Tong, B.; Yu, H.; Waterhouse, G.I.; Zhou, C.; Zhao, Y.; Tahir, M.; Wu, L.Z.; Tung, C.H.; Zhang, T. Integrating metallic nanoparticles of Au and Pt with MoS$_2$–CdS hybrids for high-efficient photocatalytic hydrogen generation via plasmon-induced electron and energy transfer. *Adv. Energy Mater.* **2016**, *6*, 1501241.

12. Zhao, X.; Liu, H.; Qu, J. Photoelectrocatalytic degradation of organic contaminants at Bi$_2$O$_3$/TiO$_2$ nanotube array electrode. *Appl. Surf. Sci.* **2011**, *257*, 4621–4624. [CrossRef]

13. Fu, H.; Pan, C.; Yao, W.; Zhu, Y. Visible-Light-Induced Degradation of Rhodamine B by Nanosized Bi$_2$WO$_6$. *J. Phys. Chem. B* **2005**, *109*, 22432–22439. [CrossRef]

14. Kudo, A.; Omori, K.; Kato, H.; Am, J. A Novel Aqueous Process for Preparation of crystal form-controlled and highly crystalline BiVO$_4$ powder from layer ed vanadates at room temperature and its photocatalytic properties. *Chem. Soc.* **1999**, *121*, 11459–11467. [CrossRef]

15. Zhang, K.; Liu, C.; Huang, F.; Zheng, C.; Wang, W. Study of the electronic structure and photocatalytic activity of the BiOCl photocatalyst. *Appl. Catal. B Environ.* **2006**, *68*, 125–129. [CrossRef]

16. Li, W.; Jia, X.; Li, P.; Zhang, B.; Zhang, H.; Geng, W.; Zhang, Q. Hollow mesoporous SiO$_2$-BiOBr nanophotocatalyst: Synthesis, characterization and application in photodegradation of organic dyes under visible-light irradiation. *ACS Sustain. Chem. Eng.* **2015**, *3*, 1101–1110. [CrossRef]

17. Wu, J.; Huang, F.; Lü, X.; Chen, P.; Wan, D.; Xu, F. Improved visible-light photocatalysis of nano-Bi$_2$Sn$_2$O$_7$ with dispersed s-bands. *J. Mater. Chem.* **2011**, *21*, 3872–3876. [CrossRef]

18. Wang, Z.; Huang, Y.; Ho, W.; Cao, J.; Shen, Z.; Lee, S.C. Fabrication of Bi$_2$O$_2$C O$_3$/g-C$_3$N$_4$ heterojunctions for efficiently photocatalytic NO in air removal: Insitu self-sacrificial synthesis characterizations and mechanistic study. *Appl. Catal. B Environ.* **2016**, *199*, 123–133. [CrossRef]

19. Kako, T.; Zou, Z.; Katagiri, M.; Ye, J. Decomposition of organic compound over NaBiO$_3$ under visible light irradiation. *Chem. Mater.* **2007**, *19*, 198–202. [CrossRef]

20. Takei, T.; Haramoto, R.; Dong, Q.; Kumada, N.; Yonesaki, Y.; Kinomura, N.; Mano, T.; Nishimoto, S.; Kameshima, Y.; Miyake, M. Photocatalytic activities of various pentavalent bismuthates under visible light irradiation. *J. Solid State Chem.* **2011**, *184*, 2017–2022. [CrossRef]

21. Wang, W.; Chen, X.; Liu, G.; Shen, Z.; Xia, D.; Wong, P.K.; Yu, J.C. Monoclinic dibismuth tetraoxide: A new visible-light-driven photocatalyst for environmental remediation. *Appl. Catal. B Environ.* **2015**, *176–177*, 444–453. [CrossRef]

22. Sun, M.; Li, S.; Yan, T.; Ji, P.; Zhao, X.; Yuan, K.; Wei, D.; Du, B. Fabrication of heterostructured Bi$_2$O$_2$CO$_3$/Bi$_2$O$_4$ photocatalyst and efficient photodegradation of organic contaminants under visible-light. *J. Hazard. Mater.* **2017**, *333*, 169–178. [CrossRef]

23. Kumada, N.; Hosoda, M.; Kinomura, N. Preparation of alkaline earth bismuth pyrochlores containing Bi^{5+} by low temperature hydrothermal reaction. *J. Solid State Chem.* **1993**, *106*, 476–484. [CrossRef]

24. Wang, X.; Liu, L.; An, H.; Zhong, Y.; Wang, D.; Tang, C.; Hu, C. (Sr$_{0.6}$Bi$_{0.305}$)$_2$ Bi$_2$O$_7$ as a new visible-light-responsive photocatalyst: An experimental and theoretical study. *Mater. Res. Bull.* **2019**, *118*, 110484. [CrossRef]

25. Liang, N.; Wang, M.; Jin, L.; Huang, S.; Chen, W.; Xu, M.; He, Q.; Zai, J.; Fang, N.; Qian, X. Highly efficient Ag$_2$O/Bi$_2$O$_2$CO$_3$ pn heterojunction photocatalysts with improved visible-light responsive activity. *ACS Appl. Mater. Interfaces* **2014**, *6*, 11698–11705. [CrossRef]

26. Zhang, X.; Zhang, J.; Yu, J.; Zhang, Y.; Cui, Z.; Sun, Y.; Hou, B. Fabrication of InVO$_4$/AgVO$_3$ heterojunctions with enhanced photocatalytic antifouling efficiency under visible-light. *Appl. Catal. B Environ.* **2018**, *220*, 57–66. [CrossRef]

27. Qu, Y.; Duan, X. Progress, challenge and perspective of heterogeneous photocatalysts. *Chem. Soc. Rev.* **2013**, *42*, 2568–2580. [CrossRef]

28. Xu, M.; Han, L.; Dong, S. Facile fabrication of highly efficient g-C$_3$N$_4$/Ag$_2$O heterostructured photocatalysts with enhanced visible-Light Photocatalytic Activity. *ACS Appl. Mater. Interfaces* **2013**, *5*, 12533–12540. [CrossRef]

29. Lin, B.; Li, H.; An, H.; Hao, W.; Wei, J.; Dai, Y.; Ma, C. Preparation of 2D/2D g-C$_3$N$_4$ nanosheet@ZnIn$_2$S$_4$ nanoleaf heterojunctions with well-designed high-speed charge transfer nanochannels towards high-efficiency photocatalytic hydrogen evolution. *Appl. Catal. B Environ.* **2018**, *220*, 542–552. [CrossRef]

30. Yang, G.; Yan, Z.; Xiao, T. Preparation and characterization of $SnO_2/ZnO/TiO_2$ composite semiconductor with enhanced photocatalytic activity. *Appl. Surf. Sci.* **2012**, *258*, 8704–8712. [CrossRef]

31. Uddin, M.T.; Nicolas, Y.; Olivier, C.; Toupance, T.; Servant, L.; Müller, M.M.; Kleebe, H.; Ziegler, J.; Jaegermann, W. Stability, durability and regeneration ability of a novel Ag-based photocatalyst $Ag_2Nb_4O_{11}$. *Inorg. Chem.* **2012**, *54*, 7764–7773.

32. Wen, X.; Niu, C.; Zhang, L.; Zeng, G. Fabrication of SnO_2 nanopaticles/BiOI n–p heterostructure for wider spectrum visible-light photocatalytic degradation of antibiotic oxytetracycline hydrochloride. *ACS Sustain. Chem. Eng.* **2017**, *5*, 5134–5147. [CrossRef]

33. Alshehri, N.; Al-Marzouki, F.; Alshehrie, A.; Hafez, M. Synthesis, characterization and band alignment characteristics of NiO/SnO_2 bulk heterojunction nano architecture for promising photocatalysis applications. *J. Alloys Compd.* **2018**, *757*, 161–168. [CrossRef]

34. Inderan, V.; Lim, S.Y.; Ong, T.S.; Bastien, S.; Braidy, N.; Lee, H.L. Synthesis and characterizations of SnO_2 nanorods via low temperature hydrothermal method. *Superlattices Microstruct.* **2015**, *88*, 396–402. [CrossRef]

35. Hu, C.H.; Zhuang, J.; Zhong, L.S.; Zhong, Y.; Wang, D.H.; Zhou, H.Y. Significantly enhanced photocatalytic activity of visible light responsive $AgBr/Bi_2Sn_2O_7$ heterostructured composites. *Appl. Surf. Sci.* **2017**, *426*, 1173–1181. [CrossRef]

36. Xia, D.; Wang, W.; Yin, R.; Jiang, Z.; An, T.; Li, G.; Zhao, H.; Wong, P.K. Enhanced photocatalytic inactivation of Escherichia coli by a novel Z-scheme $g-C_3N_4/m-Bi_2O4$ hybrid photocatalyst under visible light: The role of reactive oxygen species. *Appl. Catal. B Environ.* **2017**, *214*, 23–33. [CrossRef]

37. Tian, J.; Hao, P.; Wei, N.; Cui, H.; Liu, H. 3D Bi_2MoO_6 Nanosheet/TiO_2 Nanobelt Heterostructure: Enhanced Photocatalytic Activities and Photoelectochemistry Performance. *ACS. Catal.* **2015**, *5*, 4530–4536. [CrossRef]

38. Zheng, Y.; Zhang, X.; Zhao, J.; Yang, P. Assembled fabrication of α-Fe2O3/BiOCl heterojunctions with enhanced photocatalytic performance. *Appl. Surf. Sci.* **2018**, *430*, 585–594. [CrossRef]

39. Zhong, L.S.; Hu, C.H.; Zhuang, J.; Zhong, Y.; Wang, D.H.; Zhou, H.Y. $AgBr/MgBi_2O_6$ heterostructured composites with highly efficient visible-light-driven photocatalytic activity. *J. Phys. Chem. Solids* **2018**, *117*, 94–100. [CrossRef]

40. Yu, L.; Zhang, X.; Li, G.; Cao, Y.; Shao, Y.; Li, D. Highly efficient $Bi_2O_2CO_3/BiOCl$ photocatalyst based on heterojunction with enhanced dye-sensitization under visible light. *Appl. Catal. B Environ.* **2016**, *187*, 301–309. [CrossRef]

41. Yin, J.; Huang, S.; Jian, Z.; Wang, Z.; Zhang, Y. Fabrication of heterojunction $SnO_2/BiVO_4$ composites having enhanced visible light photocatalystic activity. *Mater. Sci. Semicond. Process.* **2015**, *34*, 198–204. [CrossRef]

42. Bai, X.; Wang, L.; Zhu, Y. Visible photocatalytic activity enhancement of $ZnWO_4$ by graphene hybridization. *ACS Catal.* **2012**, *2*, 2769–2778. [CrossRef]

43. Shi, F.; Yang, C.G.; Niu, D.W. $SrTiO_3$ nanocubes decorated with Ag/AgCl nanoparticles as photocatalysts with enhanced visible-light photocatalytic activity towards the degradation of dyes, phenol and bisphenol A. *Environ Sci.* **2017**, *4*, 585–595.

44. Xu, Y.; Schoonen, M.A.A. The absolute energy positions of conduction and valence bands of selected semiconducting minerals. *AM Miner.* **2000**, *85*, 543–556. [CrossRef]

45. Zhang, S.W.; Li, J.X.; Zeng, M.Y.; Zhao, G.X.; Xu, J.Z.; Hu, W.P. In situ synthesis of water-soluble magnetic graphitic carbon nitride photocatalyst and its synergistic catalytic performance. *ACS Appl. Mater. Interface* **2013**, *5*, 12735–12743. [CrossRef]

46. Liu, W.; Wang, M.L.; Xu, C.X.; Chen, S.F.; Fu, X.L. Ag_3PO_4/ZnO: An efficient visible-light-sensitized composite application in photocatalytic degradation of Rhodamine B with its application in photocatalytic degradation of Rhodamine B. *Mater. Res. Bull.* **2013**, *48*, 106–113. [CrossRef]